文章编号: 1001 - 9014(2018)01 - 0020 - 06

DOI:10.11972/j.issn.1001 - 9014.2018.01.005

Non-periodic wide-angle beam steering HCG array for application in VCSEL

HUANG You-Wen[1,2], ZHANG Xing[1*], ZHANG Jian-Wei[1], ZHONG Chu-Yu[1,2], LIU Ying-Ying[1,2], XIANG Lei[1,2], QIN Li[1], NING Yong-Qiang[1], WANG Li-Jun[1]

(1. State Key Laboratory of Luminescence and Applications, Changchun Institute of Optics, Fine Mechanics and Physics, Chinese Academy of Sciences, Changchun 130033, China;
2. University of Chinese Academy of Sciences, Beijing 100049, China)

Abstract: The non-periodic high-index contrast grating with a given period and duty was designed to manipulate the wave-front phase shift of the beam and further realize multi-angle beam steering. The finite difference time domain method was used to simulate the grating bars with a specific sorting order, and the beam steering angles of −10.644°, −21.176°, −28.307°, 10.644°, 21.447°, and 28.418° were obtained. Based on the multi-angle steering high contrast grating (HCG) array, a vertical cavity surface emitting laser (VCSEL) source with multi-deflection angle beam steering ability was proposed to meet the requirement of wide-field light detection and ranging (LIDAR) source. The tiny and easy integration of wide-angle emitting VCSEL light source system can cater to the compact and miniature LIDAR systems.

Key words: VCSEL, non-periodic HCGs, multi-deflection angles, optical beam manipulation, LIDAR
PACS: 42.55.Px, 42.60.Jf, 42.15.Eq

应用于 VCSEL 的宽角度光束控制非周期性高对比度光栅阵列

黄佑文[1,2], 张 星[1*], 张建伟[1], 钟础宇[1,2], 刘莹莹[1,2], 向 磊[1,2], 秦 莉[1], 宁永强[1], 王立军[1]

(1. 中国科学院长春光学精密机械与物理研究所 发光学及应用国家重点实验室,吉林 长春 130033;
2. 中国科学院大学,北京 100049)

摘要:设计了特定周期和占空比的非周期性高对比度光栅来实现光束的波前相位控制,进而实现对光束的多角度控制.在研究中,采用有限时域差分法模拟了特殊排列的非周期高对比度光栅,并获得了 −10.644°, −21.176°, −28.307°, 10.644°, 21.447°和 28.418°的光束控制角度.基于这种多角度控制的高对比度光栅阵列,提出了一种具有多角度光束控制的 VCSEL 光源,这种尺寸极小的宽角发射 VCSEL 光源系统能使激光雷达系统的结构紧凑化和微型化.

关 键 词:垂直腔面发射激光器;非周期性高对比度光栅;多偏转角度;光束控制;激光雷达

中图分类号:TN248.4 **文献标识码**:A

Introduction

Range finder and altimeter wide-field light detection and ranging (LIDAR) systems are the core components of autonomous navigation and small-unmanned aerial vehicles[1-2], driver assistance and the fully autonomous driving systems, navigation on natural targets, collision avoidance, object profiling and identification[3-4]. A number of LIDAR products sold in the market suffer from large size and expensive unit price. Furthermore, the mechanical rotating and annular distribution of multi-lasers are used to realize 360° surround view. The angle steerable semiconductor laser possesses absolute advanta-

Received date: 2017-05-14, **revised date**: 2017-08-23 **收稿日期**:2017-05-14, **修回日期**:2017-08-23
Foundation items:Supported by National Natural Science Foundation of China (61434005, 61474118, 61376070, 11404326, 61405190 and 11674314); Youth Innovation Promotion Association, CAS (2017260); Science and Technology Program of Jilin province (20150203011GX); Science and Technology Program of Changchun, China (15SS02); The National Key Research and Development Program of China (2017YFB0503200)
Biography:HUANG You-Wen (1989-), male, Zhaotong, Ph. D. candidate. Research field is VCSEL design, fabrication and surface microstructure (grating and micro-lens). E-mail: huangyouwen13@mails.ucas.ac.cn
* **Corresponding author**:E-mail: zhangx@ciomp.ac.cn

ges, such as price superiority, long lifetime, downscaled device size and high efficiency, in LIDAR system. Many methods, such as the off-chip mechanical and compact monolithic integrated methods, are currently used for beam steering. The mechanical method of the rotating polygonal mirror[5-6] results in a bulky, complicated, unstable and slow optical system. The improved methods of the monolithic steering techniques, such as the two p-type electrodes[7], photonic crystal[8] and slow-light Bragg reflector waveguide[9], avoid the troubles introduced by the mechanical method. However, the problems of narrow steering angles, limited output power and large loss are unavoidable for the aforementioned monolithic steering methods.

The non-periodic high-index contrast grating (HCG) derived from the periodic HCG[10] was designed to focus and manipulate the beam[11-12]. Moreover, the final status of the light beam was determined by the parabolic- and linear-shapes of the wave-front phase[13-14] introduced by the given grating bar combinations. Therefore, the non-periodic HCG becomes a promising technique to replace the conventional optics, such as the focusing lens and optical scanning mirrors. The maximum steering angles of 27.42° and 36.251° for the transmitted[15] and reflected[16] light were achieved through the non-periodic HCG, respectively. However, the non-periodic HCG was designed to be independent from the vertical cavity surface emitting laser (VCSEL) device and just serve as an optical element[17].

In this study, the non-periodic HCGs with multi-deflection angles were designed to manipulate the VCSEL beam through the linear phase shift on the transmission plane of the non-periodic HCG with fixed thickness. Then, a series of numerical simulations were carried out in a 2-D finite difference time domain (FDTD) model to demonstrate the feasibility of our design. Finally, a monolithic integrated non-periodic HCG VCSEL was proposed to realize the multi- and wide-angle beams steering. That inherits the simple and compact-structure of HCG[10] and VCSEL, reduces the number of lasers used, miniaturizes the size and lowers the price of the wide-field LIDAR.

1　Theory model

The phase response of the HCG is determined by the grating period (Λ), duty cycle (η), bar thickness (t_g) and the refractive index. In this study, t_g was fixed, and the refractive index of the grating bar at 1.55 μm wavelength was set as 3.48, the refractive index beneath the grating bars was set as 1. In the transmission field, electric field envelope function of the transmitted light can be expressed as[17],

$$E(x,z) = E_0(x,z)\exp[jk_0(x\sin\theta + z\cos\theta)] \quad , \quad (1)$$

where E_0 is the electric filed amplitude, $k_0 = 2\pi/\lambda$ is the wavenumber, and θ is defined as the deflection angle, which is the included angle between beam propagation direction and the normal direction of grating. z is the monitor position, and the distance is set to be 1.5μm away from the output plane in the simulation. Therefore, the phase response is an exponential function of single variable x and can be written as

$$\varphi(x) = k_0 x\sin\theta + c \quad , \quad (2)$$

where c is a constant. The deflection angle θ can be expressed as[16],

$$\theta = \arcsin(\Delta\varphi/k_0 x) \quad , \quad (3)$$

where $\Delta\varphi$ is the phase difference in the range of the width x of non-periodic HCG. Therefore, the deflection angle is determined by the $\Delta\varphi$ and width of non-periodic HCG.

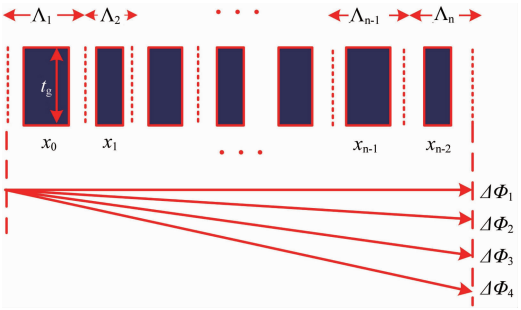

Fig. 1　The model of the non-period HCG
图 1　非周期性高对比度光栅模型

The grating bars whose period and duty cycle matched the linear phase shift were aligned into a line of finite non-periodic HCG, and the sort order follows:

$$x_{n+1} = x_n + 1/2(\Lambda_n + \Lambda_{n+1}) \quad , \quad (4)$$

where $n = 1, 2, 3, \cdots$, x_n and Λ_n are the central coordinate and periodicity of n_{th} grating bar, as shown in Fig. 1.

2　Non-periodic HCGs Design

In the present study, the thickness of the periodic HCG was fixed at 0.71 μm, the high refractive index was considered as 3.48 at 1.55 μm wavelength, and the low refractive index was 1. The high-index grating bars were surrounded by air. The rigorous coupled-wave analysis (RCWA) method was applied to calculate the transmissivity and phase on the transmission plane of periodic HCG. The period ranged from 0.2μm to 1.3μm, and the duty cycle swept from 0.2 to 0.9. The source was 1.55 μm TE polarization (the electric component parallel to the HCG bars) plane wave. Figure 2(a) shows the transmissivity contour map of the periodic HCG, and the transmissivity varies from 0 to 1. Figure 2(b) shows the phase shift contour map of the transmitted light on the transmission plane that covers a full 2π phase shift. The transmissivity and phase of the transmitted light on the transmission plane are independently determined by the discrete grating period and duty cycle.

Therefore, the grating bars that matched the designed phase curve were selected in the simulation and aligned into a non-periodic HCG structure. The total amount of phase shift is different for different deflection angles. The phase shifts for ±10°, ±20°, and ±30° deflection angles are ±7.563°, ±14.388° and ±20.792° in the range of the 10μm long non-periodic HCG, and the slopes for various deflection angles are ±0.756°/μm, ±1.439°/μm and ±2.079°/μm, respectively. Figure 3 shows the discrete grating periods and duty cycles for the six deflection angles. The x-axis represents the numbers of grating bars and sort orders. In

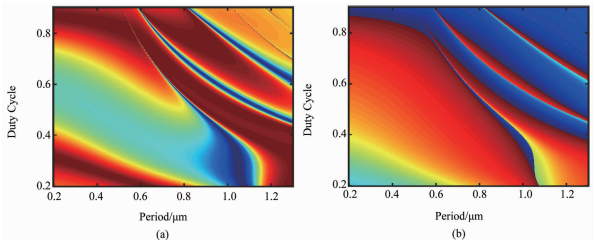

Fig. 2 The contour map of the transmissivity and phase shift of period HCG with thickness 0.71 μm
图 2 0.71 μm 厚的周期性高对比度光栅透射率和相移等值图

the design process, only three datasets of grating parameters were selected for +10°, +20° and +30° deflection angles and labeled with red, blue and green marks, respectively. The decreasing phase resulted in the negative deflection angle when the grating bars were aligned in reverse orders with respect to the sort orders of positive deflection angles. Therefore, Figures 3(a) and 3(b) show the periods and duty cycles of non-periodic HCGs for ±10°, ±20°, and ±30° deflection angles.

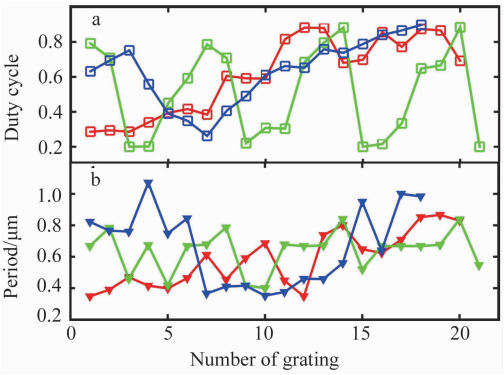

Fig. 3 The parameters of non-period HCG for different deflection angles
图 3 不同偏转角度的非周期性高对比度光栅参数

Figure 4 shows the designed phase shifts for various deflection angles. The red square and diamond dots in Figs. 4(a) and 4(b) are the phase shift on the transmission plane of non-periodic HCG for ±10° deflection angle, and the black straight lines correspond to linear fitting lines. The slopes of phase shift are −0.764°/μm and 0.852°/μm for −10° and +10°, respectively. The green square and diamond dots in Figs. 4(a) and 4(b) depict the phase shift for ±20° deflection angle, and the slopes of the two fitting lines are −1.535°/μm and 1.714°/μm, respectively. The blue square and diamond dots display the designed phase shift for ±30° deflection angle, and the slopes of their phase shift are −1.854°/μm and 1.824°/μm. A large deflection angle requires the non-periodic HCG to realize large phase shift.

3 Results and discussion

In this study, the FDTD software was applied to simulate the finite non-periodic HCG. Figure 1 shows the simulation model. In the simulation, the boundary condition was set as perfectly matched layer. A 1.55 μm TE

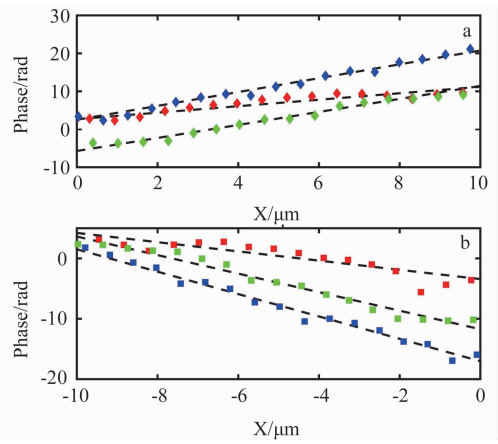

Fig. 4 The designed phase shifts for various deflection angles
图 4 多种偏转角度的相移设计

plane wave was placed beneath the grating bars. A power monitor was 1.5μm away from the HCG output surface to monitor the phase shift within the range of the non-periodic HCG. Two linear monitors were set to record the deflective electric field in the transmission region, and the deflection angles can be calculated based on the offset dimension of the maximum position of the electric field.

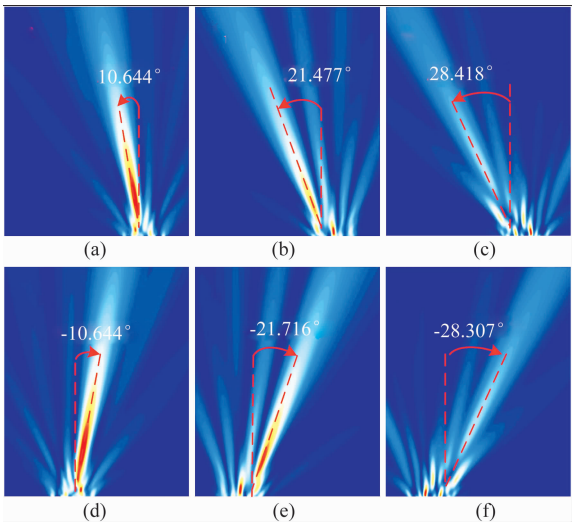

Fig. 5 The beams with different deflection angles
图 5 不同偏转角度的光束

Figure 5 shows the deflected beams that are numbered with detail deflection angles. The beam with counterclockwise deflection possesses positive deflection angle, otherwise, the deflection angle is negative. Figures 5(a), (b) and (c) display the positive deflection angle of 10.644°, 21.447° and 28.418°, which correspond to the increasing phase shift in figure 4(a), and whose periods, duty cycles and sort orders are shown in Figs. 3(a) and (b). In the range of the 10μm non-periodic HCG, the amount of the phase shift determined by the period, duty cycle and sort order defines the deflection angle. Figures 5(d), (e), and (f) shows the negative deflection angles of −10.644°, −21.176°, and

−28.307°, respectively. Moreover, their phase shift slopes are negative in Fig. 4(b), and their grating parameters and sort orders are shown in Figs. 3(a) and (b). The slopes of the designed deflection angles differ from that of the theoretical value. Thus, the simulated deflection angles deviate from the expected angles marginally.

Simultaneously, the transmissivity of the non-periodic HCG with different sort orders was calculated. The transmissivities of non-periodic HCGs for 10.644°, 21.447°, and 28.418° deflection angles are 0.787, 0.805, and 0.653, respectively, and the values for −10.644°, −21.176°, and −28.307° deflection angles are 0.754, 0.757, and 0.639, respectively. The different transmissivities result in the different E intensity of transmitted light.

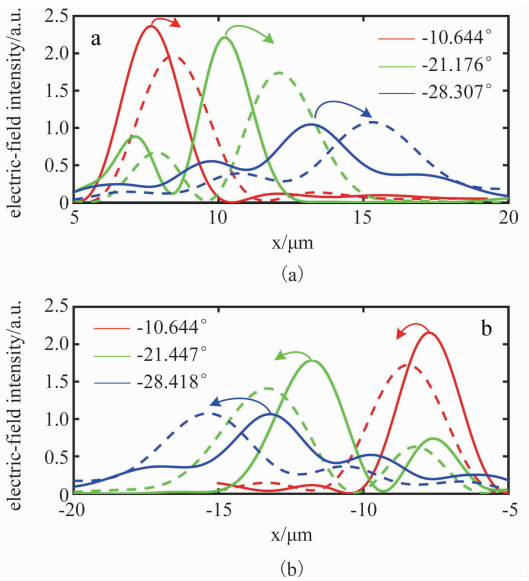

Fig. 6　The electric-field intensity of negative and positive deflection beams at different distance to be away from the transmission plane

图 6　正向偏转和负向偏转光束距离透射平面不同位置处的电场强度

Figures 6(a) and (b) show the electric field intensity of the negative and positive deflective beams that are displayed with different color solid and dash lines at different location z_1 and z_2. The x-coordinates of the maximum points that are marked by dash lines deviate from the ones marked by solid lines. The deflection angles can be calculated based on the x-offset and the interval between z_1 and z_2, and the deflection angle of θ can be expressed as $\theta = \text{atan}[(x_{x_2} - x_{x_1})/(z_2 - z_1)]$. Table 1 shows the partial simulation parameters and the simulated deflection angles.

A TE polarization non-periodic HCGs array was designed to change the beam directions of fundamental mode emitting VCSELs. Figure 7 shows the design of a multi-deflection angle VCSEL array. Every three elements in the VCSEL array are connected in series connection manner and injected current simultaneously. Figure 8 shows the monolithic VCSEL source prototype with ability of angle scanning. The six columns of the VCSELs are integrated with the non-periodic HCG with the ability of 30°, 20°, 10°, −10°, −20° and −30° deflection angle. The external high-speed pulse current is injected from the first column to the sixth column individually. Thus, the angle sweeping can be realized and a high-steering speed and wide-steering angle is sustained.

Table 1　Partial simulation parameters and the simulated deflection angles

表 1　部分模拟参数和模拟的偏转角度

Designed angle	Monitor position z/μm	Max $\lvert E \rvert^2$ at x/μm	Simulated deflected angle
−10°	14	−7.728	−10.644°
	18	−8.480	
−20°	14	−11.831	−21.176°
	18	−13.381	
−30°	14	−13.289	−28.307°
	16	−14.366	
10°	14	7.684	10.644°
	18	8.436	
20°	10	10.167	21.447°
	15	12.132	
30°	14	13.149	28.418°
	18	15.313	

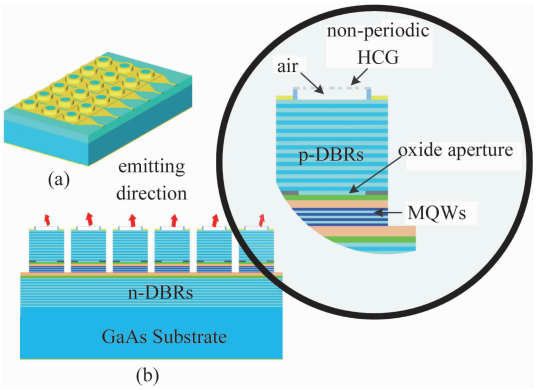

Fig. 7　The 3 × 6 angle steerable VCSELs light source (a). The front view of the VCSEL array (b). The epitaxy structure of VCSEL refers to Ref. [18]

图 7　3 × 6 角度可操纵 VCSEL 光源(a). VCSEL 列阵的前视图(b). VCSEL 外延结构[18]

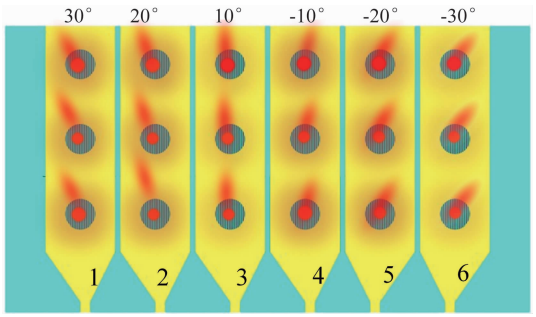

Fig. 8　The prototype of the angle scanning laser source

图 8　角度可扫激光光源原型

Figure 9 shows the polarization property of the VCSEL integrated with non-periodic HCG. The ratio of TE/

TM polarization is closed to 1. This indicates that the discrete non-periodic HCG bars integrated above the output window are not sensitive to the polarization of incident light. That means that high-transmissivity for the TE and high-reflectivity for TM polarization cannot be achieved simultaneously. The chosen discrete non-periodic HCG explains this phenomenon.

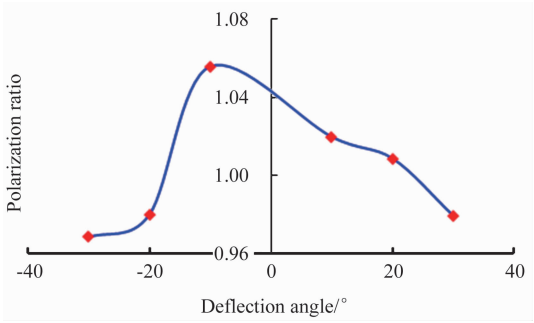

Fig. 9 Polarization selectivity of TE/TM for different discrete non-periodic HCG
图9 不同离散的非周期性高对比度光栅的 TE/TM 偏正选择性

In Fig. 10, we also analyzed the resonant wavelength of the non-periodic HCG VCSELs and the conventional VCSEL. Figures 10(a) and (c) show the resonant wavelength of the non-periodic HCG VCSELs with the ability of negative and positive deflection angle, respectively. The peak wavelength shows a red shift for ±10°, ±20° and ±30° deflection angles in comparison with the resonant wavelength of conventional VCSEL in Fig. 10(b), and the shift values increase with the increasing deflection angles. The lasing wavelength of HCG-VCSEL is required to meet the round-trip 2π phase condition, which can be expressed as Eq. 5[19],

$$4\pi \frac{L_{\text{cavity}}}{\lambda_{\text{la sing}}} + \varphi_{\text{HCG}} + \varphi_{\text{DBR}} = 2\pi m \quad , \quad (5)$$

where L_{cavity} is the physical cavity length, $\lambda_{\text{la sing}}$ is the lase wavelength, φ_{HCG} and φ_{DBR} are the phase shift introduced by HCG and DBR, respectively. All the work is done with same epitaxy structure, the L_{cavity} and φ_{DBR} influence on the peak resonant wavelength equally. Therefore, the redshift of lasing wavelength of non-periodic HCG VCSELs is determined by the different φ_{HCG}, which is introduced by different combination of discrete non-periodic HCG bars. The phase-modulated non-periodic HCG brings the non-zero phase into VCSEL and results in a shift of zero-phase point and eventually a redshift of peak wavelength.

4 Conclusions

In this study, a monolithic multi-deflection angles steering non-periodic HCG array was designed to manipulate the directions of light beam of VCSEL and the feasibility was certified by FDTD simulation. In the simulation, the simulated deflected angles of −10.644°, −21.176°, −28.307°, 10.644°, 21.447°, and 28.418° coincided with the designed deflection angles of ±10°, ±20° and ±30°. The external high-speed pulse

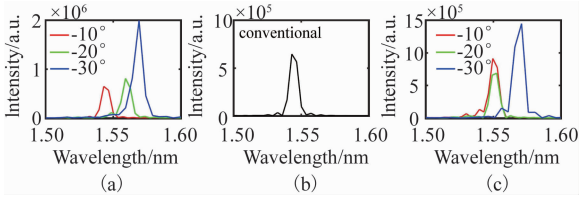

Fig. 10 Peak wavelength of non-periodic HCG VCSEL ((a) for negative deflection angle and (c) for positive deflection angle) and conventional VCSEL (b)
图10 非周期高对比度光栅 VCSEL 的峰值波长((a)负偏转角度,(c)正偏转角度),常规 VCSEL 的峰值波长(b)

current was important to realize the angle sweeping of VCSEL that was integrated with the non-periodic HCG array. In this work, a prototype of a light source with angle steering was proposed. Moreover, much HCGs with finer angle steering ability are needed to provide an enhanced resolution for the easy identification of objects.

References

[1] Geske J, Wang C, Macdougal M, *et al.* High power VCSELs for miniature optical sensors [J], *Proceedings of Spie*, 2010, 7615:76150E-76150E-11.
[2] Geske J, Macdougal M, Stahl R, *et al.* Miniature Laser Rangefinders and Laser Altimeters: Avionics, Fiber-Optics and Photonics Technology Conference. IEEE, San Diego, 2008[C]. [*s. n.*]
[3] Geske J, Macdougal M, Cole G, *et al.* High power VCSELs for smart munitions [J], *Proceedings of Spie*, 2006, **6287**:628703-628703-12.
[4] Newman Neil E, Graham Allen D C S, Mohamed A, *et al.* High Peak Power VCSELs in Short Range LIDAR Applications [J]. *Journal of Undergraduate Research in Physics*, 2013.
[5] Matsuda T, Abe F, Takahashi H. Laser printer scanning system with a parabolic mirror [J]. *Applied Optics*, 1978, **17**(6): 878-884.
[6] Wyant J C. Rotating Diffraction Grating Laser Beam Scanner [J]. *Applied Optics*, 1975, **14**(5):1057-1058.
[7] Toshihide I, Mitsuaki S, Seiji M, *et al.* Continuous Output Beam Steering in Vertical-Cavity Surface-Emitting Lasers with Two p-Type Electrodes by Controlling Injection Current Profile [J]. *Japanese Journal of Applied Physics*, 1999, **38**(4R): 1966.
[8] Siriani D, D. Choquette K. Electronically Controlled Two-Dimensional Steering of In-Phase Coherently Coupled Vertical-Cavity Laser Arrays [J]. *IEEE Photonics Technology Letters*, 2011, **23**(3):167-169.
[9] Shimada T, Matsutani A, Koyama F, *et al.* On-chip electro-thermal beam steering based on slow-light Bragg reflector waveguide laterally integrated with VCSEL: Photonics Conference, Burlingame, 2012 [C]. [*s. n.*]
[10] Zhou Y, Huang M Y C, Chase C, *et al.* High-Index-Contrast Grating (HCG) and Its Applications in Optoelectronic Devices [J]. *IEEE Journal of Selected Topics Quantum*, 2011, **15**(5):1485-1499.
[11] Fattal D, Li J, Peng Z, *et al.* Flat dielectric grating reflectors with focusing abilities [J]. *Nat Photon*, 2010, **4**(7):466-470.
[12] Lu F, Sedgwick F G, Karagodsky V, *et al.* Planar high-numerical-aperture low-loss focusing reflectors and lenses using subwavelength high contrast gratings [J]. *Optics Express*, 2010, **18**(12):12606-12614.
[13] Yang J, Wang Z, Wang F, *et al.* Atomically thin optical lenses and gratings [J]. *Light Sci Appl*, 2016, **5**: e16046.
[14] Papaioannou M, Plum E, Valente J, *et al.* Two-dimensional control of light with light on metasurfaces [J]. *Light Sci Appl*, 2016, **5**: e16070.

(下转第29页)

of $n(\omega)$ increased, and the peak position shifted to the low-energy region accompanied by significant reduction in $n(\omega)$ in the high-energy region. Figures 7(c) and (d) show $n(\omega)$ of graphene with different concentration of impurities. The maximum value of $n(\omega)$ decreased greatly, and significant increase in the refractive index was observed in the high-energy region with increase in doping concentration (50% doped). In the case of graphene doped with B, a new peak appeared in the low-energy region. In the case of graphene doped with N, the position of the peak in the low-energy region shifted towards the high-energy region direction.

The optical parameter corresponding to the refractive index is reflectivity $R(\omega)$, which is shown in Fig. 6 (e). The maximum reflectivity of pristine graphene was 0.58 at an optical energy of 22.24 eV. The reflectivity observed at optical energies above 35 eV was very small. In the case of graphene doped with B or N, the maximum value of $R(\omega)$ increased, and the peaks in the low-energy region shifted toward further lower-energy region. In addition, the optical energy range decreased to values less than 30 eV. Figures 7(e) and (f) show $R(\omega)$ of graphene with different concentration of impurities. The maximum value of $R(\omega)$ decreased, and its position shifted toward further lower-energy region with increase in doping concentration (50% doped). Furthermore, the peaks in the low-energy region shifted toward the high energy region direction.

2.3.3 Electron energy loss function

The electron energy loss (EELS) function describes the energy loss of electrons in a homogeneous medium. The peak value of the function represents plasma turbulence, and the corresponding oscillation frequency is known as the plasma frequency. The EELS is shown in Fig. 6(f). Several peaks were observed, the maximum height of the peaks was 4.64 at an optical energy of 23.24 eV for pristine graphene. In the case of graphene doped with B or N, only one obvious peak was observed in the same position as the maximum height of pristine graphene, and the height of this peak increased significantly; the peak position corresponds to the edge energy of plasma and indicates the transition point from a semimetallic to semi-conductor material. This indicates that the presence of B or N in the graphene reduces plasma excitation in the low-energy region and part of high-energy region. The plasma excitation peaks increased, and the EELS peak broadened; the height of the peaks decreased significantly with increase in doping concentration (50% doped).

3 Conclusions

Based on the first principle density functional theory calculation, the electronic and optical properties of graphene doped with B and N are investigated in this study. The electronic and optical properties of graphene were regulated significantly by B or N doping. The band gap was opened and increased with an increased in doping concentration. Interaction between the impurities and C atom, causing charge transfer, were observed. The changes in the optical properties occurred mainly in the low-energy region, the curves of these parameters shrunk in the high-energy region. The peaks of the optical parameters in the low energy region shifted toward the high energy region with the increase in the doping concentration (50% doped), and the peaks of some parameters in the low-energy region disappeared, as seen from the EELS.

References

[1] WANG Xin-Ren, DAI Hong-Jie. Etching and narrowing of graphene from the edges [J]. Nature Chemistry. 2010, **2**: 661 - 665.

[2] JIAO Li-Ying, WANG Xin-Ran, Diankov G, *et al*. Facile synthesis of high-quality graphene nanoribbons [J]. Nature Nanotechnology. 2010, **5**:321 - 325.

[3] YUN Jiang-Ni, ZHANG Zhi-Yong, YAN Jun-Feng, *et al*. First-principles study of B or Al-Doping effect on the structural, electronic structure and magnetic properties of γ-graphene [J]. Computational Materials Science. 2015, **108**:147 - 152.

[4] ZHANG Yuan-Bo, TANG Tsung-Ta, Girit C, *et al*. Direct observation of a widely tunable bandgap in bilayer Graphene [J]. Nature, 2009, **459**: 820 - 823.

[5] Robertson A W, Montanari B, He K, *et al*. Dynamics of single Fe atoms in graphene vacancies[J]. Nano Letters. 2013, **13**(4):1468 - 1475.

[6] Crook C B, Constantin C, Ahmed T, *et al*. Proximity-induced magnetism in transition metal substituted graphene [J]. Scientific Reports. 2015, **5**:12322.

[7] Nossa J F, Naumov I I, Cohen R E. Effects of manganese addition on the electronic structure of BaTiO3 [J]. Physical Review B. 2015, **91**(21): 214105.

[8] JIA Yan-Jun, DU Yu-Jie, WANG Mei-Shan. First-principles studies of electronic structure and optical properties of GaN surface doped with Si [J]. Optik. 2014, **125**: 2234 - 2238.

[9] Ebnonnasir Abbas, Narayanan Badri, Kodambaka Suneel, *et al*. Tunable MoS2 bandgap in MoS2-graphene heterostructures [J]. APPLIED PHYSICS LETTERS. 2014, **105**: 031603.

[10] Panchakarla L S, Subrahmanyam K S, Saha S K, et al. Synthesis, structure, and properties of boron-and nitrogen-doped graphene [J]. Adv. Mater. 2009, **21**:4726.

[11] ZHANG Yun-Qiu, LIANG Yong-Ming, ZHOU Jian-Xin. Recent Progress of Graphene Doping [J]. Acta Chim. Sinica. 2014, V72(3): 367 - 377.

[12] SHENG Zhen-Hua, GAO Hong-Li, BAO Wen-Jing. Synthesis of boron doped graphene for oxygen reduction Reaction in fuel cells [J]. Mater. Chem. 2012, V22(2):390 - 395.

(上接第 24 页)

[15] Ma C, Huang Y, Duan X, *et al*. High-transmittivity non-periodic subwavelength high-contrast grating with large-angle beam-steering ability [J]. *Chinese Optics Letters*, 2014, **12**(12):120501 - 120501.

[16] fang w, Huang Y, Ma C, *et al*. *High-contrast-gratings reflector based on SOI with large-angle beam steering ability*: Asia Communications and Photonics Conference, Shanghai, 2014[C]. [*s. n.*]

[17] Fang W, Huang Y, Duan X, *et al*. Non-periodic high-index contrast gratings reflector with large-angle beam forming ability [J]. *Optics Communications*, 2016, **367**:6 - 11.

[18] Faez R, Marjani A, Marjani S. Design and simulation of a high power single mode 1550nm InGaAsP VCSELs [J]. *IEICE Electron Express*, 2011, **8**(13):1096 - 1101.

[19] Karagodsky V, Pesala B, Chase C, *et al*. Monolithically integrated multi-wavelength VCSEL arrays using high-contrast gratings [J]. *Optics Express*, 2010, **18**(2): 694 - 699.